Lab on a Chip

Accepted Manuscript

ROYAL SOCIETY OF CHEMISTRY

www.rsc.org/loc

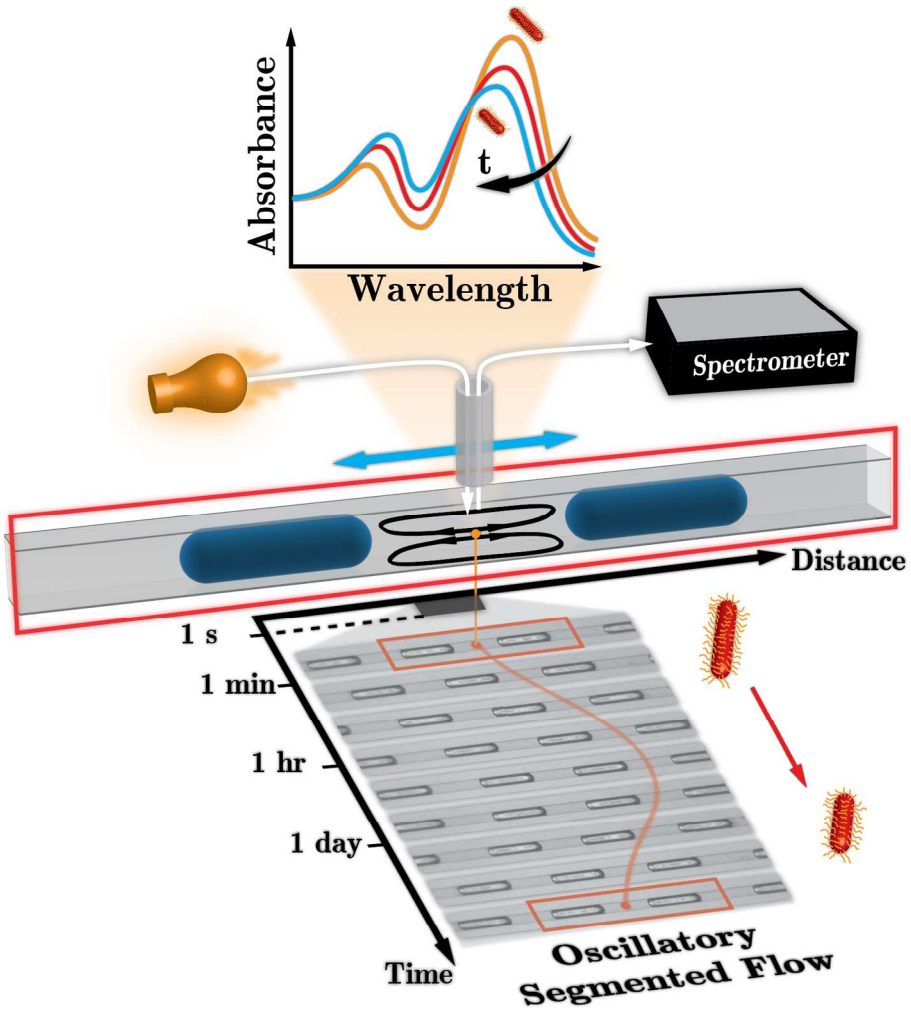

Shaken and Stirred: Oscillatory Segmented Flow for Controlled Size-Evolution of Colloidal Nanomaterials

Milad Abolhasani [a], Ali Oskooei [a], Anna Klinkova [b], Eugenia Kumacheva [b,c] and Axel Günther [a,c]*

[a] *Department of Mechanical and Industrial Engineering, University of Toronto, Toronto, ON, M5S 3G8, Canada. Fax: (416)978-3356; Tel: (416)978-1282; E-mail: axel.guenther@utoronto.ca*
[b] *Department of Chemistry, University of Toronto, Toronto, ON, M5S 3H6, Canada. Fax: (416)978-3356; Tel: (416)978-3576; E-mail: ekumache@chem.utoronto.ca*
[c] *Institute of Biomaterials & Biomedical Engineering, University of Toronto, 164 College Street, Toronto, Ontario, M5S 3G9, Canada.*

Abstract

We introduce *oscillatory segmented flow* as a compact microfluidic format that accommodates slow chemical reactions for the solution-phase processing of colloidal nanomaterials. The strategy allows the reaction progress to be monitored at a dynamic range of up to 80 decibel (i.e., residence times of up to one day, equivalent to 720-14400 times the mixing time) from only one sensing location. A train of alternating gas bubbles and liquid reaction compartments (segmented flow) was initially formed, stopped and then subjected to a consistent back-and-forth motion. The oscillatory segmented flow was obtained by periodically manipulating the pressures at the device inlet and outlet via square wave signals generated by non-wetted solenoid valves. The readily implementable format significantly reduces the device footprint as compared with continuous segmented flow. We investigated mixing enhancement for varying liquid segment lengths, oscillation amplitudes and oscillation frequencies. The etching of gold nanorods served as a case study to illustrate the utility of the approach for the dynamic characterization and precise control of colloidal nanomaterial size and shape during 5 hrs. Oscillatory segmented flows will be beneficial for a broad range of lab-on-a-chip applications that require long processing times.

1. Introduction

Over the past decade, flow chemistry platforms[1-3] have been utilized to characterize chemical reaction mechanisms,[4-6] screen physical[7-10] and chemical[11, 12] properties of reagents, optimize reaction conditions,[11] and prepare colloidal materials in a scalable manner[13-16]. In particular, microscale segmented flow reactors which resemble a miniature train of continuous stirred-tank reactors, have been employed to continuously perform a variety of rapid physical [8, 10] and chemical [17-23] applications with processing times shorter than 5min. Figure 1a illustrates such gas-liquid or liquid-liquid segmented flow approaches with typical reaction volumes of ~0.1mL per channel and an additional volume of 0.1-1mL potentially associated with downstream characterization using a flow cell[24-27]. Enhanced mass transport is a key advantage of segmented flow microreactors compared to their single phase flow counterparts[28] which allows for mixing times, t_M, between tens of milliseconds and several seconds [18, 20, 29-31]. However, numerous candidates of slow chemical reactions and mass transfer processes including the solution-phase preparation of spherical nanoparticles[32, 33] and nanorods,[34-37] atomic transfer radical polymerizations[38, 39] and protein crystallization,[40, 41] currently cannot be meaningfully translated into continuous segmented flow formats. Accommodating a desired processing time, t_R, for a given total volumetric flow rate (i.e., continuous plus dispersed phase), Q, and a microchannel cross-section, A, a microchannel with a length of $L=t_R Q A^{-1}$ is required (Figure 1a). At long processing times, the device footprint and fabrication cost increase linearly with L. For processing times between 30 min and 1 day and typical flow rates of 5-100 μL/min, prohibitively large device footprints would be required. The use of segmented flow reactors is therefore limited to processing times shorter than 5 min, microchannel lengths of L=1-100 cm [8] and device footprints of 10-20 cm^2. The distance-to-time-transformation in segmented flows further implies reaction dynamics to be acquired from multiple measurements obtained at different positions along the microchannel. However, obtaining measurements (e.g., UV-visible, fluorescence, Fourier

transform-infrared or nuclear magnetic resonance spectroscopy, temperature and pH [26]) at multiple downstream locations is often challenging to implement and requires dedicated microreactor or probe designs. Even if realized, the discrete number of measurement locations limits the addressable dynamic range. [42, 43]

Here, we introduce *oscillatory segmented flow* as a strategy that offers direct and independent control over t_M and t_R, and allows the shapes of solution-processed nanoparticles to be monitored, with a large dynamic range and at a single sensing location only. A segmented gas-liquid segmented flow was initially formed using passive breakup and then subjected to oscillatory motion by periodically modulating the pressures at both microchannel ends.

Recently, Gielen *et al.* [44] and Jakiela *et al.* [45] reported two approaches for oscillatory droplet flows. Gielen *et al.* [44] induced oscillatory flow of droplets within a tube by manipulating the continuous phase flow to investigate the kinetics of an enzymatic reaction with a dynamic range of 6 dB. Jakiela *et al.* [45] conducted oscillatory droplet flow by actuating custom electromagnetic valves and investigated bacterial growth in a thermoplastic-based microfluidic device with a dynamic range of 80 dB. While emulsification of reagents within a droplet drastically reduces axial dispersion, the compartmentalization of reaction volumes within a continuous, immiscible liquid imposes a few limitations that do not exist if an inert gas is used as the segmenting fluid. For instance, droplet-based systems require surfactants to be added, provide only limited access to the oscillating droplet reactors while a reaction is progressing and require a dedicated separation step in order to breakdown the emulsion after processing has been completed. However, employing an inert gas as the segmenting fluid as well as the fluid that induces oscillatory motion eliminates these limitations and significantly extends the practicality of the oscillatory segmented flow approach.

As schematically shown in Fig. 1b, oscillatory segmented flow reduces the required microfluidic device footprint for slow processes such as nanoparticle growth and shape

control at time scales between 10 minutes and 1 day with dynamic ranges of up to 80 dB. In section 2, we demonstrate our experimental setup. In section 3, we characterize flow and mixing behavior in oscillatory segmented flow and present controllable etching of gold nanorods as a case study that serves to illustrate the utility of oscillatory segmented flows in guiding the evolution of nanoparticle shapes.

2. Experimental

Materials. Mineral Oil (light oil, Sigma Aldrich Canada, Oakville, ON, Canada) and ethyl alcohol (100%, Commercial Alcohols, Toronto, ON, Canada) were used as working liquids in the mixing characterization experiments. A yellow color oil soluble fluorescent dye (DFSB-K43, Risk Reactor Inc., Santa Ana, CA, USA) was used to quantify mixing in oscillatory segmented flow. Cetyl trimethyl ammonium bromide (CTAB), gold chloride ($HAuCl_4$), sodium borohydride ($NaBH_4$), sodium oleate, Silver nitrate ($AgNO_3$), ferric chloride (FeCl3) were purchased from Sigma Aldrich Canada.

Flow Control. The microfluidic platform employed in this study is schematically shown in Fig. 2. Four digital pressure regulators (Type 3410, full scale 0-5 psig (0-34.47 kPag), accuracy 0.5%FS, Marsh Bellofram, Newell, WV, USA) were connected to a gas cylinder (Helium, Grade 3, Linde BOC, Canada) to supply the constant upper gas pressure level, P_{0H}, and the lower gas pressure level, P_{0L}. Two electromagnetic valves (The Lee Company, Westbrook, CT, USA) were used to establish square waveform pressure signals at the device inlet and outlet. Two syringe pumps modules (OEM high-pressure module, Harvard Apparatus, Holliston, MA, USA), were used for priming the device by initially establishing a regular segmented gas-liquid flow. The syringe pumps, the digital pressure regulators and the electromagnetic valves were all controlled by a custom software program [10, 46] (version LabVIEW 2010, National Instruments, Austin, TX, USA) and a data acquisition board (model USB 6008, National Instruments). Two inlets of each electromagnetic valve were connected

to the outlet of the two digital pressure regulators that maintained P_{0H} and P_{0L}, while their common outlets were connected to the gas inlet and the pressurized reservoir at the device outlet. The computer-controlled operation of the electromagnetic valves enabled us to apply square waveform pressure inputs with a fixed amplitude and variable frequency and duty cycle at the inlet and the outlet of the microfluidic device.

Imaging. A high power white fluorescent lamp and a UV filter cube were used for fluorescent imaging of the PDMS-based microfluidic device (Device 1) in an inverted fluorescent microscope (model TE-2000-S, Nikon Instruments Inc., Melville, NY, USA). A cooled and intensified charged coupled device (CCD) camera (model QICAM FAST1394, QImaging, Surrey, BC, Canada) in combination with a white diffusive on-axis light source (model Smart Series DOAL 50 mm-White, Microscan Systems Inc., Renton, WA, USA) were used for bright-field imaging of segmented and oscillatory segmented flows within a silicon-based microfluidic device (Device 2).

Microfabrication. The experiments were conducted using microfluidic devices that were fabricated in two different substrate materials: poly dimethyl-siloxane (PDMS) and silicon. The PDMS-based microfluidic device (Device 1) was microfabricated using soft lithography.[47] By utilizing photolithography, the designed microchannel pattern was transferred to a 150 μm thick layer of a negative photoresist (SU-8 2050, MicroChem Corp., Newton, MA, USA), which was uniformly spun on a 2" × 3" glass microscope slide (Corning Inc., Corning, NY, USA). The molded PDMS layer, contained the desired microchannel network (multiphase section: width, W=300 μm, height, H=150 μm and L=0.15 m), was then peeled off and plasma bonded to a 1-mm thick glass microscope slide. The silicon-based microfluidic device (Device 2) was microfabricated using shadow mask lithography, and front and back side deep reactive ion etching (DRIE). Details of the microfabrication process flow and the device integration are described elsewhere.[8]

On-Chip Spectroscopy. A 50 μm thick premium-grade bifurcated optical fiber (QBIF50-UV-VIS, Ocean Optics Inc., Dunedin, FL, USA) in combination with a Tungsten Halogen light source (HL-2000-LL, Ocean Optics Inc., Dunedin, FL, USA) and a UV-Vis miniature fiber optic spectrometer (USB 4000, detector range: 200-1100 nm, signal to noise ratio: 300:1, pixel size: 8μm×200 μm, Ocean Optics Inc., Dunedin, FL, USA) were used for on-chip UV-Vis absorbance evolution of gold nanorods during the etching process within a silicon-based microfluidic device (Device 2). The bifurcated configuration of the fibers allowed us to use an opaque substrate (silicon) and take advantage of the light reflection inside the microchannel to increase the light path-length. Water was injected into the microfluidic device, and its corresponding absorption intensity was used as the reference spectra.

Synthesis of Gold Nanorods. Gold nanorods were synthesized according to a recently reported procedure [48] using a binary surfactant mixture. The seed solution was prepared by the reduction of $HAuCl_4$ (0.12 mL, 15 mM) in 2.5 mL of 0.2 M aqueous solution of CTAB with 0.6 mL of 10mM cold $NaBH_4$. The seeds were aged for 30 min before use. To prepare the growth solution, 0.28 g of CTAB and 0.05 g of sodium oleate were dissolved in 10 mL of water in a 25 mL Erlenmeyer flask followed by the addition of 0.29 mL of 10 mM $AgNO_3$ solution. After 15 min of incubation at 30^{o}C, 10 mL of 1 mM $HAuCl_4$ solution was added followed by stirring the mixture for 90 min at room temperature after which the solution became colorless. At this point, 0.12 mL of concentrated HCl (12 M) was added to the growth solution followed by the addition of 1.25 mL of 0.064 M ascorbic acid. To initiate nanorod growth, 0.03 mL of seed solution was injected into the growth solution, which was then stirred for 30 seconds and left undisturbed at 30^{o}C for 12 hours. The resultant solution of nanorods was used without further purification or size/shape-selective fractionation.

3. Results and Discussion

In this section we report the mixing characteristics associated with oscillatory gas-liquid segmented flows and apply the concept to the solution processing of colloidal nanoparticles.

3.1 Characterization of Oscillatory Segmented Flow

In this section, we evaluate the dynamics of the oscillatory motion of a liquid segment using a time series of bright-field images. Four digital pressure regulators supplied a constant upper gas pressure level, P_{0H}, and a lower gas pressure level, P_{0L} (Figure 2). Two electromagnetic valves allowed square waveform pressure signals to be applied at the device inlet and outlet, P_{inlet} and P_{outlet}, respectively.

The following experimental sequence was used to establish oscillatory segmented flows:

(i) *Continuous Segmented Flow:* Two syringe pumps that supplied the to-be-mixed liquid streams were set at a constant flow rate. The gas inlet and the device outlet pressures were fixed at the constant values of P_{0H} and P_{0L}, respectively. A regular segmented flow that consisted of a succession of uniformly sized gas plugs and liquid segments was obtained as shown in Figure 2 (i).

(ii) *Oscillatory Segmented Flow:* After a regular segmented flow was established, the syringe pumps were stopped, and the outlet pressure was then increased from P_{0L} to P_{0H} to stop the motion of liquid segments. To establish the oscillatory segmented flow, as shown in Figure 2 (ii), a square waveform was then applied to the pressures at both microchannel ends with $P_{inlet}(t)$ and $P_{outlet}(t)$ having a duty cycle of 50% and a phase shift of 180°.

The time series of micrographs in Figure 3a shows two liquid segments that are entrapped between inert gas plugs while carrying out one oscillation cycle (See Movie M1). A custom developed image processing code (Matlab R2011A, Mathworks, Natick, MA, USA) allowed the positions of the gas plugs along the microchannel to be extracted from the acquired bright-field images. For each image frame, the locations of the plug caps were associated with the local intensity maxima as evaluated along the microchannel center line. By subtracting the

locations of the right cap, $X_{R,}$ and the left cap, X_L, of a gas plug we determined the plug length, $L_{B,i}= X_{R,i}-X_{L,i}$, the liquid segment length, $L_{S,i}=X_{L,i}-X_{R,i-1}$, and the center position of the liquid segment, $X_{C,i}=0.5[X_{L,i}+X_{R,i-1}]$ at each instant of time. Figures 3b and 3c show the time-dependence of $L_B(t)$ and L_S (t) during 30 oscillation cycles. The corresponding values for a much longer time period that corresponded to 86,400 oscillation cycles, equivalent to a dynamic range of 80 dB, are shown in Fig. S1. The data illustrate that L_B and L_S remained constant during one day of uninterrupted oscillatory segmented flow operation within a gas impermeable silicon-based microfluidic device (Device 2).

At each instant in time, X_C was associated with the velocity of the liquid segment, U_C, as calculated by the difference between the liquid segment center positions in two subsequent frames divided by the time delay between two frames, dt. Figures 3d and 3e show the measurement results for $X_C(t)$ and $U_C(t)$ as evaluated for two sets of pressures P_{0H} and P_{0L}. While some irregularities are found in the position of the liquid segment (Fig. 3d), the corresponding velocity profiles exhibit a quasi-periodic behavior (Fig. 3e) for the selected operating conditions. Fast-Fourier transforms (FFT) were applied to $X_C(t)$ and $U_C(t)$. The resulting frequency spectra are shown in Fig. S2 and exhibit a dominant frequency of 0.5 Hz, suggesting a quasi-harmonic behavior for displacement and velocity of the liquid segment during its oscillatory motion. The frequency spectrum also suggests that a reduced pressure difference (P_{0H} - P_{0L}) results in a closer-to-harmonic behavior of U_C.

3.2 Characterization of Oscillatory Mixing

In the next step, we utilized the oscillatory segmented flow strategy as a method of mixing two miscible liquids: fluorescently labeled and optically clear mineral oil. Figure 4a shows a time-series of fluorescent micrographs for a liquid segment consisting of a clear top half and fluorescently labeled bottom half during one oscillation cycle (See Movies M2, M3 and M4). Figure 4b shows the computed velocity fields in a mineral oil segment, during one oscillation

cycle, obtained by a 2-D numerical simulation (Comsol Multiphysics 4.3a, Burlington, MA, USA), within a non-inertial frame of reference (attached to the liquid segment). Owing to the small (~0.08) Reynolds number, *Re*, associated with the oscillatory segmented flows studied here, the effect of inertial forces compared to the viscous forces were assumed to be negligble. As shown in Fig. 4b, the streamline velocities follow a harmonic behavior during the oscillatory motion (see Movie M5). Figure 4c shows the concentration evolution of the fluorescent dye corresponding to the velocity fields displayed in Fig. 4b. Further detail on the simulation is available in the ESI (S-3).

Oscillatory segmented flow promotes mixing as compared to purely diffusive transport between two co-flowing liquids due to a periodic recirculation inside each liquid segment. Two axisymmetric recirculation zones are formed inside a liquid segment as illustrated in Fig. 4b. The recirculation zones enhance mixing by constantly translating and stretching the liquid along with solute molecules contained in it, within the top and the bottom halves of the liquid segment. Mixing behaviour has been extensively studied in the context of gas-liquid segmented flows[31, 49, 50] or rectangular cavities[51-54]. The time it takes for two miscible liquids to mix in the segmented flow configuration is generally governed by the time required for the solute molecules to travel along the recirculation zones formed in the liquid segment, referred to as the *recirculation time.* Thulasidas *et al.*[50] suggested the recirculation time in a square microchannel at capillary numbers $<10^{-2}$ to be constant and equal to the time required for the liquid segment to travel a distance equal to three times its length. The relatively large aspect ratio (190) of the liquid segments used in this study did not allow the effect of microchannel width to be investigated. However, Ottino *et al.*[51, 52] found for aspect ratios <20, the recirculation time (mixing time) to be a decreasing function of the liquid segment aspect ratio.

In oscillatory segmented flow, the magnitude of the recirculation velocity at a fixed microchannel position within a liquid segment is not time constant. In order to explain how the experimentally measured mixing times depend on the oscillation frequency and the liquid

segment length, we define a "stirring strength" as $S = fd/2(L_S+W)$, where d is the distance that a liquid segment travels during one full oscillation cycle. The stirring strength is directly proportional to the distance travelled by the liquid segment in the unit time (here 1s), and represents the number of full recirculations inside the liquid segment over the unit time.

Figure 4d shows the experimentally measured fluorescent intensity, across the channel width at position X_C, normalized by the spatial average of the fluorescent intensity $\langle I \rangle_{all}(t)$ evaluated over the entire projection of a segment, X : (X_L, X_R) and Y : (0, H):

$$I^*(Y,t)\big|_{X_C} = \frac{I(Y,t)\big|_{X_C}}{\langle I \rangle_{all}(t)}. \quad (1)$$

To characterize the mixing behavior associated with oscillatory segmented flow, we evaluated the average fluorescent intensity within the clear half of the liquid segment, normalized by $\langle I \rangle_{all}(t)$:

$$\langle I^* \rangle_{top}(t) = \frac{I(X,Y,t)\big|_{X:(X_L,X_R)}^{Y:(0.5H,H)}}{\langle I \rangle_{all}(t)}. \quad (2)$$

A liquid segment is assumed to be uniformly mixed when $\langle I^* \rangle_{top}(t)$ approaches a constant value of 0.5, where $\langle I^* \rangle_{all-clear} = 0$ and $\langle I^* \rangle_{all-labeled} = 1$ correspond to intensities of the optically clear and the fluorescently labelled liquids, respectively. Figure 4e shows the time evolutions of $\langle I^* \rangle_{top}(t)$ and normalized fluorescent intensity of the entire segment,

$$\langle I^* \rangle_{all}(t) = \frac{\langle I \rangle_{all}(t)}{\langle I^* \rangle_{all-labeled} - \langle I^* \rangle_{all-lclear}}. \quad (3)$$

As shown in Fig. 4e, $\langle I^* \rangle_{all}(t)$ remains constant at 0.5 during the experiment, confirming the conservation of the fluorescent molecules within a liquid segment.

The mixing time was defined as the time required for the normalized fluorescent intensity within the clear half of the liquid segment to reach 99% of its final value (0.5). We evaluated t_M as a function of the oscillation frequency and the liquid segment length.

In a first set of experiments, L_S, P_{0L} and P_{0H} were maintained constant while f was altered. Figure 5a shows $\langle I^* \rangle_{top}$ as a function of time for L_S=1.2 ± 0.1 mm and frequencies that varied between 0.5 Hz and 500 Hz for purely diffusive mixing in the same liquid segment. The values of t_M were extracted from Fig. 5a for the different frequencies, normalized by the diffusive mixing time, t_D, and plotted in the Fig. 5b for oscillation frequencies between 0.5 Hz and 5 Hz. Normalized mixing times for a larger range of oscillation frequencies f are summarized in Fig. S5 in ESI. By increasing f from 0.5 Hz to 50 Hz, the ratio t_M/t_D initially decreased, assumed minimum of 0.1 at f=3Hz and gradually increased again at higher frequencies. As shown in Fig. 5b, by increasing f, the stirring strength initially increased, assumed a maximum at f=3 Hz, and decreased thereafter. We attribute the latter effect to the decrease in the total distance the liquid segment travels per unit time, which resulted in reduced convective mixing within the liquid segment. The displacement distance and velocities, the total displacement of the segment center during one oscillation cycle, and the corresponding frequency spectra of the displacement curves are summarized in Figs. S6 and S7 in ESI for four different frequencies. These data show that increasing the oscillation frequency from f=0.5 Hz to 5 Hz, results in a decreased amplitude of $X_C(t)$, while the amplitude of $U_C(t)$ remains constant. We attribute this effect to the fact that the same gas pressure levels were applied at the device inlet and outlet, resulting in identical steady state velocities for all the experiments independent of f. Therefore, increasing f decreased the travel time of the liquid segments while maintaining the steady state velocity and decreased the displacement amplitude. Moreover, the waveform of the liquid segment during its oscillatory motion could be tuned towards more harmonic behavior, as shown in Figs. S6 and S7, either

by tuning the PID settings of the digital servo pressure controller or by adding a capacitance between the digital servo pressure controller and the electromagnetic valve to dampen the initial effect of switching between the atmospheric pressure and P_{0H}.We define the time t_{RT} as the time required for the liquid segment velocity to assume 95% of its steady state value. According to Fig. S6c in ESI, t_{RT} = 200 ms was obtained from 1800 image frames acquired at dt =33.3 ms. Figure S6d in ESI shows the dimensionless distance travelled by the liquid segment during one full oscillation cycle for different values of f. The displacement amplitude decreases with increasing f, a finding that is consistent with the above explanation.

Next, we experimentally evaluate the effect of L_S (or the aspect ratio) on mass transport. Figure 5c shows $\left\langle I^* \right\rangle_{top}(t)$ for different values of L_S while keeping f, P_{0H} and P_{0L} constant. The corresponding dimensionless mixing times are shown in Fig. 5d. The displacement of the liquid segment, the steady state velocity and the maximum velocity remained the same for the considered values of L_S.

By increasing L_S from 0.8 mm to 3.1 mm, the normalized mixing time increased from t_M = 0.14 to 0.48 (Fig. 5d). We attribute the increase in t_M and the associated decrease in the mass transport efficiency with the behavior of S (L_S/W) shown in Fig. 5d that is in line with the prediction by Ottino *et al.*[51] for liquid segments with increasing aspect ratios. Since all liquid segments had similar travel distances (the same gas pressure levels were used), increasing L_S decreased S and thereby increased t_M/t_D. We conclude that smaller values of L_S promote mixing in oscillatory segmented flow for constant f and liquid segment displacement.

Even though segmented flows exhibit a significantly reduced effect of axial dispersion in comparison with single phase flows, neighbouring liquid segments and contained solutes do communicate via thin liquid films that surround the gas plugs. Such segment-to-segment communication occurs in the presence of a concentration gradient between the neighbouring segments. The liquid film thickness and its capillary number dependency have been studied

extensively. [50, 55-58] It has been shown that the axial dispersion in a continuous segmented flow is mainly a function of the liquid-to-gas feed flow rate ratio and the gas plug velocity. [56, 59, 60]

3.3 Case Study: Shape Control of Gold Nanorods

In this section, we utilized the oscillatory segmented flow strategy for continuously monitoring the UV-Vis absorption spectra of gold nanorods during etching. As shown in Fig. 2b, by positioning a bifurcated optical fiber directly above a 300 μm wide and 300 μm deep microchannel (see Movie M6 and Fig. S8 in ESI), the absorption spectra originating from gold nanorods within a liquid segment were monitored in real-time. Alignment of the bifurcated fiber is straightforward in comparison with a pair of single-stranded fibers and does not require complicated microfabrication steps for fiber positioning.

We prepared water-soluble gold nanorods with a mean length and width of 115nm and 27nm, respectively, stabilized with a binary surfactant mixture of cetyl trimethyl ammonium bromide (CTAB) and sodium oleate, according to a previously reported procedure [48]. As synthesised nanorods were subjected to selective chemical etching at the nanorod tips by ferric chloride solution ($FeCl_3$) [61]. Fe^{2+} ions oxidize Au^0 to Au^+ in the presence of complexing ligands (halide ions) resulting in etching of nanorods. This process preferentially occurs along the longitudinal axis of the nanorods due to the higher reactivity of (111) facets of the nanorods and weaker surface passivation of the nanorod tips owing to their greater curvature.

The etching rate was controlled by the volume ratio of gold nanorod solution to etching agent solution, *R*. The raw UV-Vis absorbance signal (Fig. S9 in ESI) detected by the miniature spectrometer was fitted to a 9^{th} order polynomial curve to reduce the noise and measure the transverse surface plasmon resonance (TSPR) and longitudinal surface plasmon resonance (LSPR) peaks of the nanorods on-chip. Figures 6a and 6b show on-chip real-time monitoring of UV-Vis absorption spectra of the nanorods with the same initial size (115 nm wide and 27 nm thick) and oscillation frequency and different *R*. Figure 6c shows the

variation of the LSPR peak wavelength, λ_P, for the gold nanorods during the etching process with varying R. As expected, smaller R (i.e. a lower concentration of the etching solution) resulted in a lower etching rate than at a higher R.

Initially, the nanorods exhibited two absorption peaks located at 862 and 520 nm, corresponding to the TSPR and LSPR, respectively. Upon etching, the LSPR peak of the nanorods blue shifted and decreased in magnitude, while the TSPR stayed nearly invariant, leading to a decrease in the aspect ratio of the nanorods. At a later stage of the process when nanorods approach a nearly isotropic shape, there is a significant decrease in the intensity of both peaks until they finally disappear due to the complete dissolution of the nanoparticles.

The results of in-situ UV-Visible spectroscopy were supported by off-chip nanorod characterization. Following a particular etching time, the oxidizing agent (Fe^{2+} ions) and halide ions were removed from the solution, by centrifugation at 5000 rcf for 5 min and re-dispersion of the nanorods in deionized water, thereby terminating the process. The purified nanorods were characterized by transmission electron microscopy (TEM). Based on the TEM image analysis, a significant shortening of the nanorods in the course of etching process was achieved from the initial nanorod length of 115 nm to 80 and 50 nm after 60 and 110 min etching, respectively (Figs 6d, 6e and 6f, respectively), while the width of the nanorods did not change after 80 min etching, confirming our claim of controlled anisotropic etching of the nanorods.

3. Summary and Conclusions

We demonstrated the complete separation of the mixing and the processing (residence) times in an approach that is independent of the microchannel length. We achieved the desired effect by establishing oscillatory motion for an initially formed and subsequently stopped segmented gas-liquid flow via periodically alternating the pressures at the inflow and outflow ends. Oscillatory flow enhanced the mixing of two miscible fluids. We studied the effects of

the oscillation frequency and the length of the liquid segments on mixing time. We introduced the "stirring strength" that quantifies mixing behavior and is defined as the displacement of the liquid segment over the unit time, normalized by the liquid segment size. Increasing the oscillation frequency from 0.5 Hz, while maintaining the liquid segment length and the inlet and outlet pressure levels, initially increased the stirring strength due to a larger total displacement per unit time, and then begun to decrease beyond the oscillation frequency of 3 Hz. However, increasing the liquid segment length (or, the liquid segment aspect ratio) while keeping the oscillation frequency and the gas pressure levels constant, decreases the stirring strength and thereby increases the time required for mixing.

The accomplished separation between the processing time and the microchannel length (i.e., residence time) reduces the required device footprint by at least one order of magnitude and removes the residence time limitation associated with flowable microfluidic systems. Long residence times associated with slow chemical or physical processes can therefore be accommodated within a small device footprint. As a case study, we successfully utilized the oscillatory segmented flow platform for on-chip monitoring of gold nanorods etching via in-situ UV-Visible spectroscopy, and demonstrated the effect of etching agent concentration on the etching rate of the nanorods.

We believe oscillatory segmented flows will significantly expand the addressable parameter space for the controlled preparation of colloidal nanomaterials in microfluidic platforms. Beyond the demonstrated case study, this approach will be relevant for the control of nanoparticle shape and the synthesis and assembly of heterostructures and may find broad applications in microfluidic chemical and materials synthesis.

Acknowledgements

We acknowledge the Bert Wasmund Graduate Fellowship in Sustainable Energy Research and Russell A. Reynolds Graduate Fellowship in Thermodynamics (MA), an Alexander Graham Bell Canada Graduate Scholarship from the Natural Sciences and Engineering Research Council of Canada (AO), Carbon Management Canada (EK), the Wallace G. Chalmers Chair of Engineering Design (AG), NSERC Discovery, Discovery Accelerator and Strategic Projects program awards, an Connaught Innovation Award and an Ontario Early Researcher Award. Device microfabrication was carried out at the CFI/ORF funded Centre for Microfluidic Systems in Chemistry and Biology (University of Toronto, Toronto, ON) and the McGill Nanotools facility (McGill University, Montreal, QC).

References

1. R. L. Hartman, J. P. McMullen and K. F. Jensen, *Angewandte Chemie International Edition*, 2011, 50, 7502-7519.
2. K. Jähnisch, V. Hessel, H. Löwe and M. Baerns, *Angewandte Chemie International Edition*, 2004, 43, 406-446.
3. K. S. Elvira, X. C. i Solvas, R. C. R. Wootton and A. J. deMello, *Nat Chem*, 2013, 5, 905-915.
4. J. Kobayashi, Y. Mori, K. Okamoto, R. Akiyama, M. Ueno, T. Kitamori and S. Kobayashi, *Science*, 2004, 304, 1305-1308.
5. N. de Mas, A. Günther, M. A. Schmidt and K. F. Jensen, *Industrial & engineering chemistry research*, 2008, 48, 1428-1434.
6. D. Voicu, C. Scholl, W. Li, D. Jagadeesan, I. Nasimova, J. Greener and E. Kumacheva, *Macromolecules*, 2012, 45, 4469-4475.
7. S. G. R. Lefortier, P. J. Hamersma, A. Bardow and M. T. Kreutzer, *Lab on a Chip*, 2012, 12, 3387-3391.
8. M. Abolhasani, M. Singh, E. Kumacheva and A. Günther, *Lab on a Chip*, 2012, 12, 1611-1618.
9. R. Sun and T. Cubaud, *Lab on a Chip*, 2011, 11, 2924-2928.
10. M. Abolhasani, M. Singh, E. Kumacheva and A. Gunther, *Lab on a Chip*, 2012, 12, 4787-4795.
11. W. Li, K. Liu, R. Simms, J. Greener, D. Jagadeesan, S. Pinto, A. Günther and E. Kumacheva, *Journal of the American Chemical Society*, 2011, 134, 3127-3132.
12. D. Voicu, M. Abolhasani, R. Choueiri, G. Lestari, C. Seiler, G. Menard, J. Greener, A. Guenther, D. W. Stephan and E. Kumacheva, *Journal of the American Chemical Society*, 2014, 136, 3875-3880.
13. J. J. Agresti, E. Antipov, A. R. Abate, K. Ahn, A. C. Rowat, J. C. Baret, M. Marquez, A. M. Klibanov, A. D. Griffiths and D. A. Weitz, *Proceedings of the National Academy of Sciences*, 2010, 107, 4004-4009.
14. N. de Mas, A. Günther, T. Kraus, M. A. Schmidt and K. F. Jensen, *Industrial & engineering chemistry research*, 2005, 44, 8997-9013.
15. W. Li, H. H. Pham, Z. Nie, B. MacDonald, A. Güenther and E. Kumacheva, *Journal of the American Chemical Society*, 2008, 130, 9935-9941.
16. M. Al-Rawashdeh, F. Yu, T. A. Nijhuis, E. V. Rebrov, V. Hessel and J. C. Schouten, *Chemical Engineering Journal*, 2012, 207–208, 645-655.
17. B. K. H. Yen, A. Günther, M. A. Schmidt, K. F. Jensen and M. G. Bawendi, *Angewandte Chemie*, 2005, 117, 5583-5587.
18. M. R. Bringer, C. J. Gerdts, H. Song, J. D. Tice and R. F. Ismagilov, *Philosophical Transactions of the Royal Society of London. Series A: Mathematical, Physical and Engineering Sciences*, 2004, 362, 1087-1104.
19. C. J. Gerdts, V. Tereshko, M. K. Yadav, I. Dementieva, F. Collart, A. Joachimiak, R. C. Stevens, P. Kuhn, A. Kossiakoff and R. F. Ismagilov, *Angewandte Chemie International Edition*, 2006, 45, 8156-8160.
20. I. Shestopalov, J. D. Tice and R. F. Ismagilov, *Lab on a Chip*, 2004, 4, 316-321.
21. H. Song, D. L. Chen and R. F. Ismagilov, *Angewandte Chemie International Edition*, 2006, 45, 7336-7356.
22. S. Duraiswamy and S. A. Khan, *Small*, 2009, 5, 2828-2834.
23. S. A. Khan, A. Günther, M. A. Schmidt and K. F. Jensen, *Langmuir*, 2004, 20, 8604-8611.
24. N. Zaborenko, E. R. Murphy, J. G. Kralj and K. F. Jensen, *Industrial & Engineering Chemistry Research*, 2010, 49, 4132-4139.

25. S. Krishnadasan, R. J. C. Brown, A. J. deMello and J. C. deMello, *Lab on a Chip*, 2007, 7, 1434-1441.
26. J. Greener, E. Tumarkin, M. Debono, C.-H. Kwan, M. Abolhasani, A. Guenther and E. Kumacheva, *Analyst*, 2012, 137, 444-450.
27. J. P. McMullen and K. F. Jensen, *Annual Review of Analytical Chemistry*, 2010, 3, 19-42.
28. T. M. Squires and S. R. Quake, *Reviews of Modern Physics*, 2005, 77, 977-1026.
29. A. D. Stroock, S. K. W. Dertinger, A. Ajdari, I. Mezić, H. A. Stone and G. M. Whitesides, *Science*, 2002, 295, 647-651.
30. I. Glasgow, J. Batton and N. Aubry, *Lab on a Chip*, 2004, 4, 558-562.
31. A. Günther, M. Jhunjhunwala, M. Thalmann, M. A. Schmidt and K. F. Jensen, *Langmuir*, 2005, 21, 1547-1555.
32. C. N. R. Rao, S. R. C. Vivekchand, K. Biswas and A. Govindaraj, *Dalton Transactions*, 2007, DOI: 10.1039/b708342d, 3728-3749.
33. M. Brust, J. Fink, D. Bethell, D. J. Schiffrin and C. Kiely, *Journal of the Chemical Society, Chemical Communications*, 1995, DOI: 10.1039/c39950001655, 1655-1656.
34. X. Lu, M. Rycenga, S. E. Skrabalak, B. Wiley and Y. Xia, *Annual Review of Physical Chemistry*, 2009, 60, 167-192.
35. X. Huang, S. Neretina and M. A. El-Sayed, *Advanced Materials*, 2009, 21, 4880-4910.
36. Liu and P. Guyot-Sionnest, *The Journal of Physical Chemistry B*, 2005, 109, 22192-22200.
37. B. Nikoobakht and M. A. El-Sayed, *Chemistry of Materials*, 2003, 15, 1957-1962.
38. M. R. Tomlinson and J. Genzer, *Macromolecules*, 2003, 36, 3449-3451.
39. Y.-Y. Tong, Y.-Q. Dong, F.-S. Du and Z.-C. Li, *Macromolecules*, 2008, 41, 7339-7346.
40. B. Zheng, J. D. Tice, L. S. Roach and R. F. Ismagilov, *Angewandte Chemie International Edition*, 2004, 43, 2508-2511.
41. C. L. Hansen, E. Skordalakes, J. M. Berger and S. R. Quake, *Proceedings of the National Academy of Sciences*, 2002, 99, 16531-16536.
42. J. Yue, F. H. Falke, J. C. Schouten and T. A. Nijhuis, *Lab on a Chip*, 2013, DOI: 10.1039/c3lc50876e.
43. J. Keybl and K. F. Jensen, *Industrial & Engineering Chemistry Research*, 2011, 50, 11013-11022.
44. F. Gielen, L. van Vliet, B. T. Koprowski, S. R. A. Devenish, M. Fischlechner, J. B. Edel, X. Niu, A. J. deMello and F. Hollfelder, *Analytical Chemistry*, 2013, 85, 4761-4769.
45. S. Jakiela, T. S. Kaminski, O. Cybulski, D. B. Weibel and P. Garstecki, *Angewandte Chemie*, 2013, 125, 9076-9079.
46. A. Oskooei, M. Abolhasani and A. Gunther, *Lab on a Chip*, 2013, 13, 2519-2527.
47. Y. Xia and G. M. Whitesides, *Annual review of materials science*, 1998, 28, 153-184.
48. X. Ye, C. Zheng, J. Chen, Y. Gao and C. B. Murray, *Nano Letters*, 2013, 13, 765-771.
49. P. Garstecki, M. A. Fischbach and G. M. Whitesides, *Applied Physics Letters*, 2005, 86, 244108-244103.
50. T. C. Thulasidas, M. A. Abraham and R. L. Cerro, *Chemical Engineering Science*, 1997, 52, 2947-2962.
51. V. S. Chakravarthy and J. M. Ottino, *Chemical Engineering Science*, 1996, 51, 3613-3622.
52. W.-L. Chien, H. Rising and J. M. Ottino, *Journal of Fluid Mechanics*, 1986, 170, 355-377.
53. J. Ottino, *Annual Review of Fluid Mechanics*, 1990, 22, 207-254.
54. J. Ottino, C. Leong, H. Rising and P. Swanson, *Nature*, 1988, 333, 419-425.

55. D. M. Fries, F. Trachsel and P. R. von Rohr, *International Journal of Multiphase Flow*, 2008, 34, 1108-1118.
56. M. T. Kreutzer, A. Gunther and K. F. Jensen, *Analytical Chemistry*, 2008, 80, 1558-1567.
57. F. P. Bretherton, *Journal of Fluid Mechanics*, 1961, 10, 166-188.
58. P. Aussillous and D. Quere, *Physics of Fluids*, 2000, 12, 2367-2371.
59. M. Muradoglu, A. Gunther and H. A. Stone, *Physics of Fluids*, 2007, 19, 072109-072111.
60. A. Gunther and K. F. Jensen, *Lab on a Chip*, 2006, 6, 1487-1503.
61. R. Zou, X. Guo, J. Yang, D. Li, F. Peng, L. Zhang, H. Wang and H. Yu, *CrystEngComm*, 2009, 11, 2797-2803.

Figures

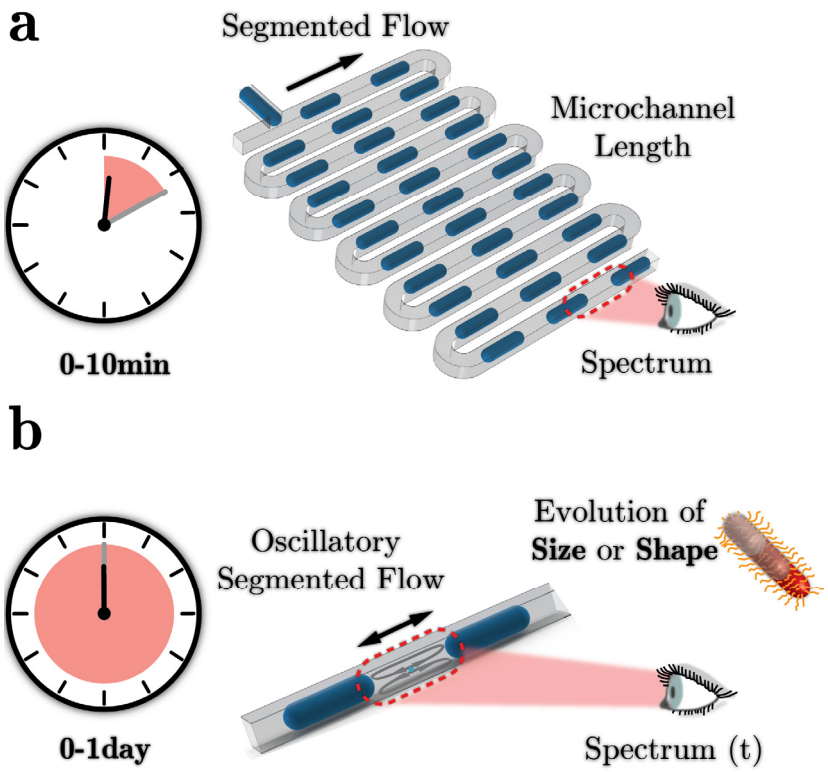

Figure 1. (a) Schematic illustration of continuously flowing gas-liquid segmented flow. Mass transfer behavior within liquid segments can be understood as a train of miniature stirred tank reactors moving at a constant velocity in the direction of flow. The measured desired parameter (e.g. spectrum) only contributes to one specific time because of the flowable format. (b) Schematic illustration of mass transfer behavior in oscillatory segmented flow as a train of stirred-tank reactors in periodic back-and-forth motion along the microchannel. In oscillatory segmented flow, the temporal evolution of the desired parameter (spectrum) can be acquired by monitoring only one location. Arbitrary values of t_R can be accommodated.

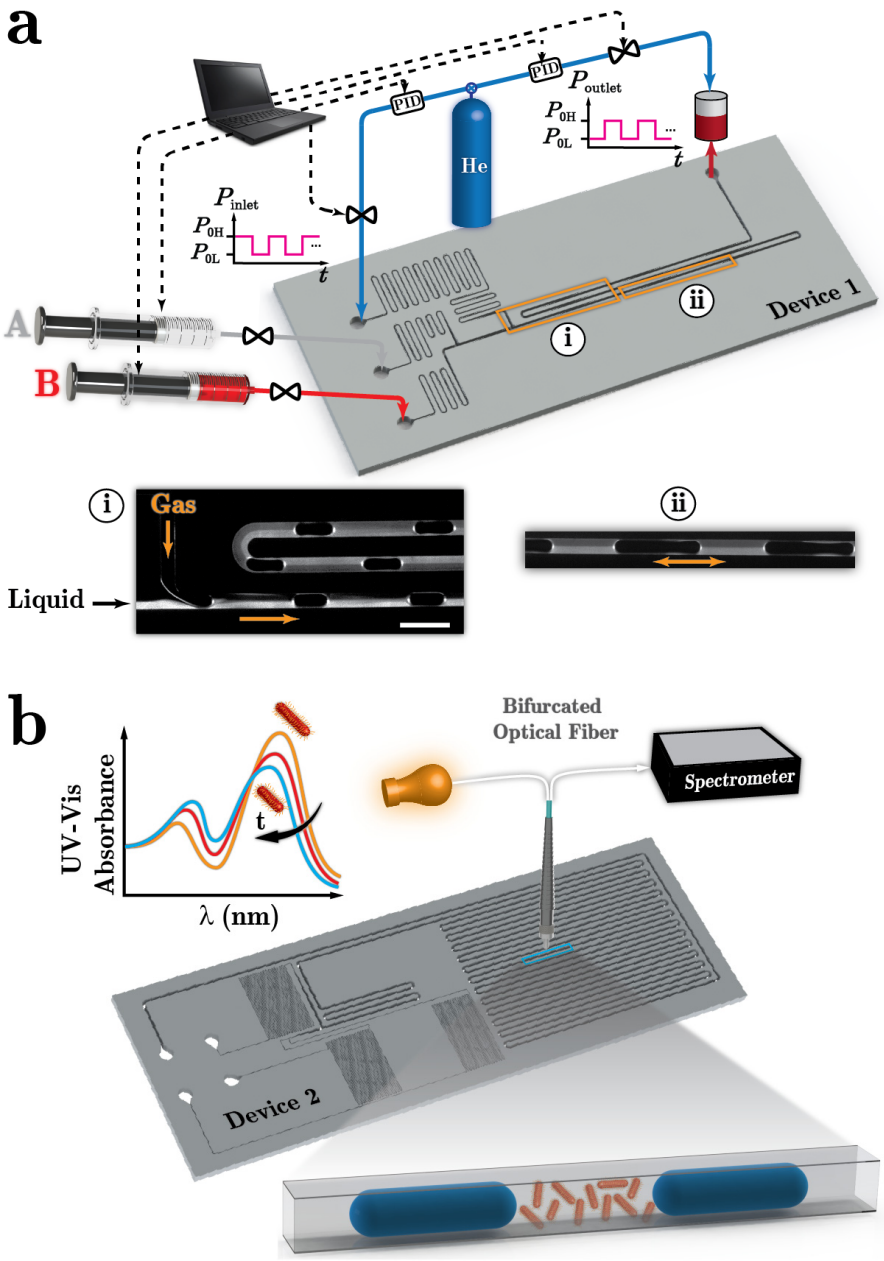

Figure 2. (a) Schematic illustration of the experimental setup including device 1, four digital pressure regulators with built-in PID controllers, two syringe pumps, and a pressurized reservoir at the outlet. Inset (1) shows a typical fluorescent micrograph of a continuous gas-liquid segmented flow with two miscible liquid streams: clear (A) and fluorescently labelled (B) mineral oil. Inset (2) shows the oscillatory segmented flow location. Scale bar is 1 mm. (b) Schematic illustration of on-chip monitoring of the absorption spectrum, on device 2, associated with solution-processed nanoparticles. Measurements are performed in reflective mode using a bifurcated single-mode fiber that guides the illuminating light from a halogen lamp to the interrogation volume of the microchannel and guides the reflected light to a miniature UV-Vis spectrometer.

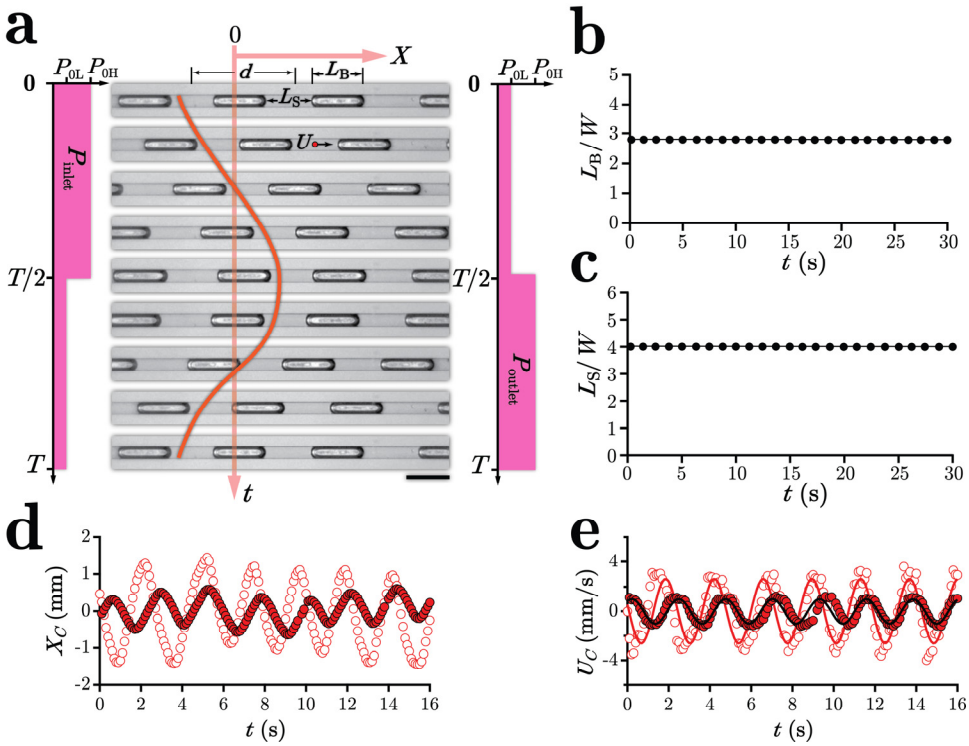

Figure 3. (a) Bright field images of one complete oscillation cycle with f=1 Hz at T=298 K including profiles of inlet and outlet pressures alternating between P_{0H} =14.48 kPag, and P_{0L} =6.89 kPag. The oscillatory segmented flow parameters L_B, L_S, d and U are highlighted. Scale bar is 1mm. (b) Nitrogen plug and (c) ethanol slug lengths variations over 30 oscillation cycles. (d) Liquid slug center X-positions with time and (e) corresponding velocities during consecutive oscillation cycles: (●) f=0.5 Hz, P_{0H}=14.48 kPag, P_{0L}=12.41 kPag; (○) f=0.5 Hz, P_{0H}=14.48 kPag, P_{0L}=6.89 kPag. 300 images with dt=0.1 were used for each experiment. Device 2 and ethanol-nitrogen pair were used for all the experiments.

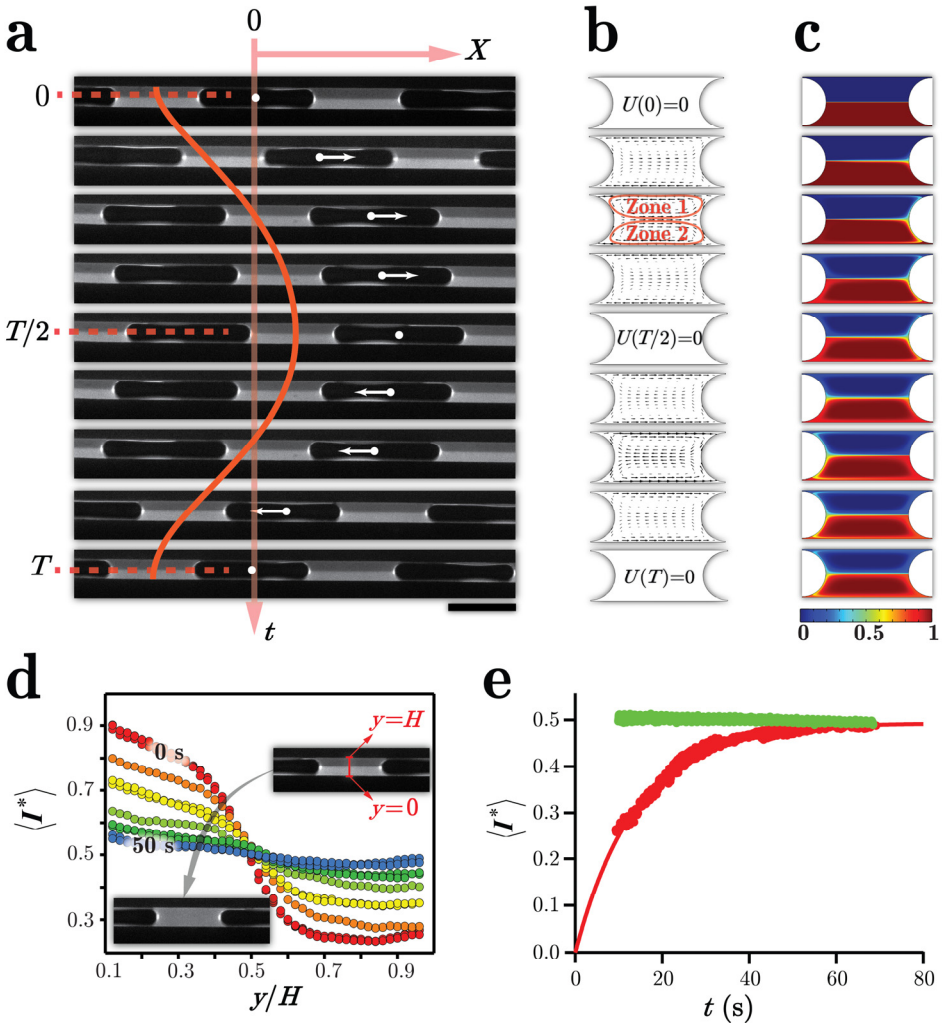

Figure 4. (a) Experimentally obtained fluorescent images of one complete oscillation cycle with f=1 Hz at T=298 K: Bottom half mineral oil containing the tracer of concentration 10 mM with the molecular weight of 324.42 g/mol and the top half is pure mineral oil. Scale bar is 1 mm. (b) Numerically predicted instantaneous velocity fields for one mineral oil segment entrapped between two inert gas plugs during one oscillation cycle. (c) Numerically predicted concentration evolution associated with the velocity fields in (b). (d) Time evolution of the normalized fluorescent intensity at the center of the liquid segment from Y=0 to Y=H, for 150 oscillation cycles at f=2 Hz, P_{0H}=12.41 kPag, and P_{0L}=0.0 kPag. Time increment between the measured data is 10 s. (e) Time evolution of the normalized fluorescent intensity average across (●) the unlabeled half and (●) the whole mineral oil segment for f=4 Hz, P_{0H}=12.41 kPag, and P_{0L}=0.0 kPag. 1800 images with dt=33.3 ms were used for (d) and (e). Device 1 and mineral oil-helium pair were used for experiments in (a), (d) and (e).

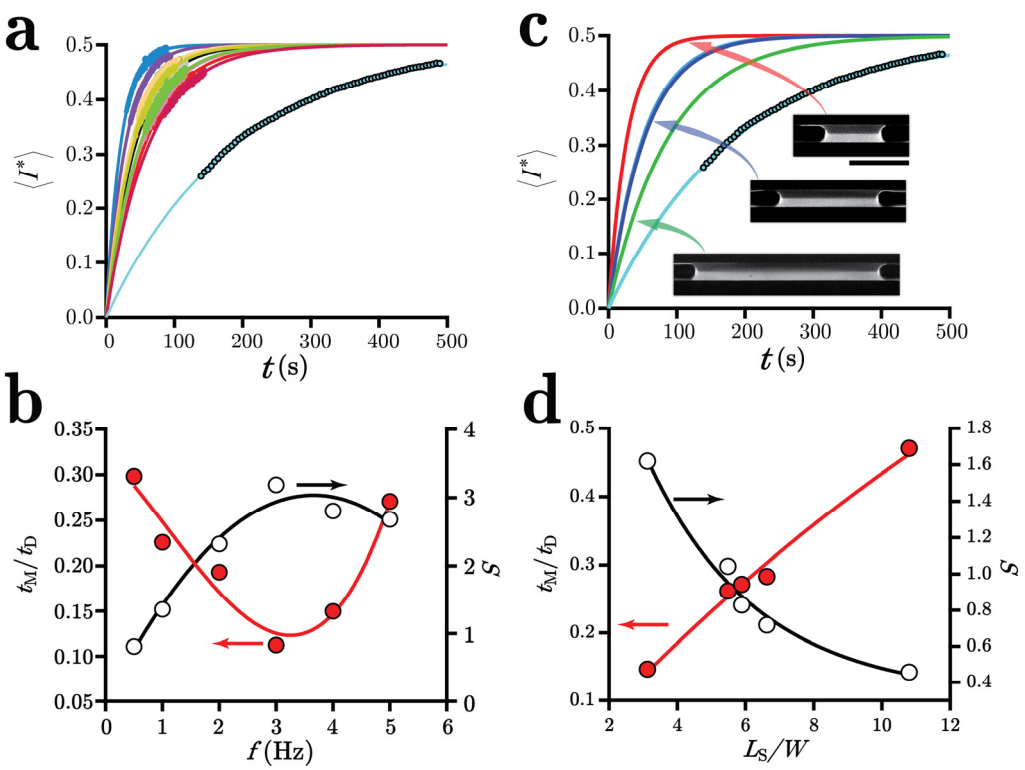

Figure 5. (a) Time evolution of the normalized fluorescent intensity for the clear half of the liquid segment with L_S =1.2±0.1 mm, P_{0H}=8.96 kPag, P_{0L}=0.0 kPag and the frequencies (●) f=0.5 Hz, (●) f=1 Hz, (●) f=2 Hz, (●) f=3 Hz, (●) f=4 Hz, (●) f=5 Hz, (●) f=10 Hz, (●) f=20 Hz, (●) f=50 Hz, (●) f=500 Hz. (●) Case of diffusion only. Measured diffusion time and diffusivity of fluorescent dye in mineral oil were 865 s and 2.6 e-11 m^2/s, respectively. (b) Frequency dependency of normalized mixing time and stirring strengths for frequencies between 0.5 Hz and 5 Hz. (c) Time evolution of normalized fluorescent intensity of the clear half of the liquid segment for varying L_S and f=1 Hz, P_{0H}=8.96 kPag and P_{0L}=0.0 kPag: (●) L_S/W=3.23, (●) L_S/W=6.16, (●) L_S/W=6.62, (●) L_S/W=10.57 and (●) diffusion only. dt=33.3 ms. Insets show three fluorescnet images of different liquid segment lengths used in this set of experiments. Scale bar is 1mm. (d) Normalized mixing time and stirring strength for different L_S. All experiments were conducted in device 1, using mineral oil-helium pair.

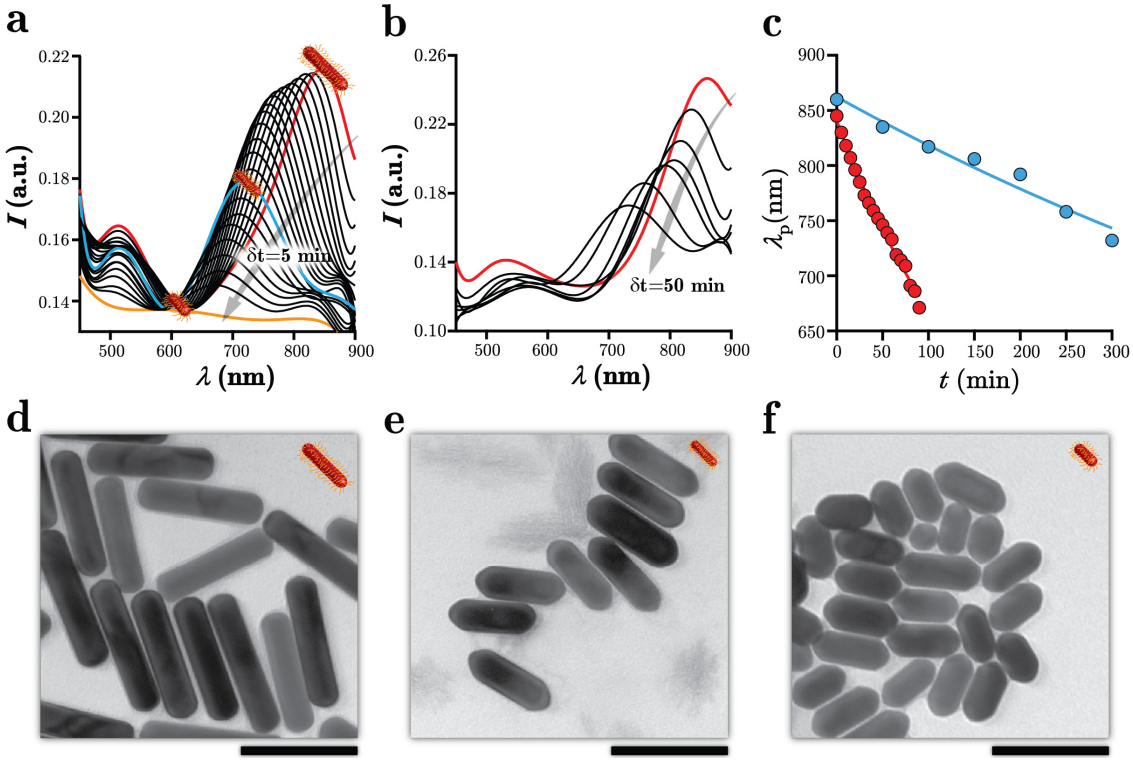

Figure 6. On-chip UV-Vis absorption spectra evolution of gold nanorods during the etching process with 0.1 M $FeCl_3$ as the etching agent for (a) R=1, f=1 Hz, P_{0H}=10.34 kPag, P_{0L}=0.0 kPag, integration time=41 ms, and L_S=2.7 mm, and (b) R=2, f=1 Hz, P_{0H}=10.34 kPag, P_{0L}=0.0 kPag, integration time=38 ms, and L_S=2.9 mm. Waiting time between each absorption read out was set at 5 min and 50 min for (a) and (b) respectively. (c) Time evolution of corresponding LSPR peak wavelength of gold nanorods associated with (a) ● and (b) ●. TEM images of (d) the initial gold nanorods, λ_P=862 nm, and etched nanorods after (e) 60 min, λ_P=717 nm, and (f) 110 min, λ_P=580 nm. Scale bars in (d), (e) and (f) are 100 nm. Experiments in (a), (b) and (c) were conducted in device 2, using helium as the inert gas plugs.